Seismic performance of circular concrete-filled steel tube columns reinforced with inner latticed steel angles

Zi-Ming Yang[1], Ju Chen[1], Fangying Wang[2], Jun Wang[3, 4]*

1. Institute of Structural Engineering, Zhejiang University, Hangzhou 310058, Zhejiang, China
2. Department of Civil Engineering, University of Nottingham, Nottingham, United Kingdom
3. Department of Civil Engineering, Hangzhou City University, Hangzhou 310015, Zhejiang, China
4. Guangdong Province Key Laboratory of Durability for Marine Civil Engineering, College of Civil and Transportation Engineering, Shenzhen University, 3688 Nanhai Avenue, Shenzhen 518060, Guangdong, China

Abstract: The seismic behavior of circular concrete-filled steel tube (CFST) columns with inner latticed steel angles under combined axial load and reversed cyclic horizontal load was studied in this paper. A total of 8 specimens was tested, including two CFST specimens and six latticed steel angles reinforced CFST specimens. The main parameters studied were the diameter-to-thickness ratio of steel tube, the cross-sectional area of inner latticed steel angles and the axial compression ratio. Firstly, the load-displacement curves and load-strain curves were obtained experimentally; secondly, the failure modes, hysteretic behaviour, skeleton curves, stiffness degradation, ductility index, hysteretic energy dissipation capacity were analyzed; thirdly, the seismic performance of the tested specimens were simulated by the established finite element (FE) models, and parametric studies were subsequently performed; finally, the modified calculation method for the horizontal bearing capacity was proposed. The research results showed that the failure of the composite columns was caused by the local buckling of the latticed steel angles and steel tube, and the latticed steel angles could effectively participate in the overall loading process. It was also found that latticed steel angles are able to improve the energy dissipation capacity.

Keywords: Seismic behavior; CFST; Latticed steel angles; Finite element models; Energy dissipation capacity.

---

* Corresponding author. Tel.: +86-151 5808 1657
E-mail address: wangjun123@szu.edu.cn (Jun Wang)

1 Introduction

Concrete-filled steel tube (CFST) is a structural element with concrete filled into steel tube, which fully utilizes the composite effect between concrete and steel. The CFSTs have the advantages of high bearing capacity, good ductility, excellent anti-seismic performance, and CFSTs are widely used in civil engineering in recent years [1]-[3]. Steel-reinforced CFST (SRCFST) is a novel structural form by internally arranging various forms of steel stiffeners [4]-[7] (such as I-section steel, crossed I-section steel, latticed steel angles and steel tubes). The steel stiffeners of the novel structure can effectively improve the mechanical properties such as strength and stiffness [4]-[7]. Among the typical cross-section types of SRCFST members shown in Fig. 1, the CFSTs with internal latticed steel angles shown in Fig. 1(d) have been successfully applied to the world's highest transmission tower in Zhejiang Province, China [8]. In engineering practice, the steel stiffeners shown in Fig. 1(a)~Fig. 1(c) may have the difficulties of positioning and construction [9]. In contrast, the internal latticed steel angles (Fig. 1(d)) have the advantages of excellent cross-sectional mechanical properties, easy positioning and convenient construction [10].

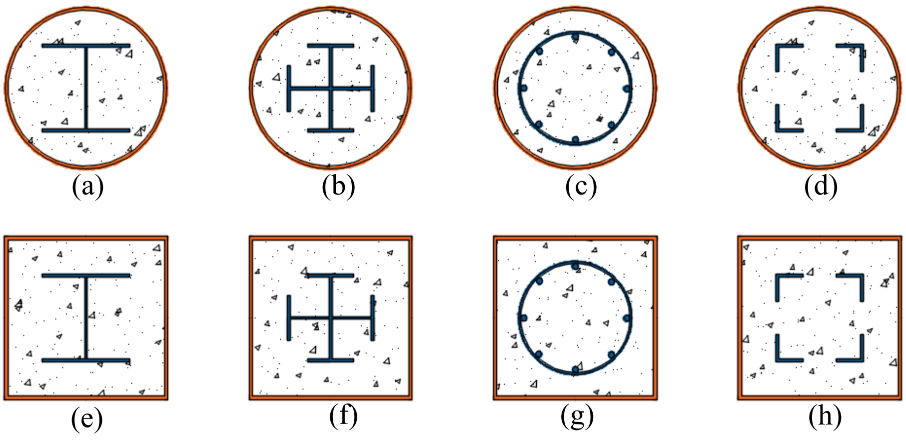

Fig. 1 Typical cross-section types of CFSTs with internal steel stiffeners

Many scholars have conducted the research on the SRCFSTs and examined their static mechanical properties via experiments, however, the understanding of the seismic performance of SRCFSTs is still insufficient. Nonetheless, some researchers have examined the hysteretic behavior of CFSTs with internal stiffeners. Specifically, Gan and Zhou [11]-[12] studied the hysteretic behavior of circular and square CFSTs with internal I-section steel, the experimental results showed that the bearing capacity increased with increasing the axial compression ratio, and the plastic deformation capacity and ductility decreased with increasing the axial compression ratio. Chang et al. [13] examined the hysteretic performance of circular CFSTs with inner I-shaped steel by numerical simulation, the parameters included the axial compression ratio, steel ratio, diameter-to-thickness ratio and concrete strength, the tests showed that the stiffness, ultimate load and deformation capacity of the SRCFSTs were higher than counterpart CFSTs. Hu et al. [14] studied the seismic performance of square CFSTs reinforced with internal spiral reinforcement, the influence of the axial compression ratio and concrete strength were analyzed, the test results showed that the internal spiral reinforcement could counteract the reduction of ductility caused by the increase of axial compression ratio, and the increase of concrete strength had no obvious influence on the deformation capacity. Ding et al. [15] studied the hysteretic behavior of circular and square CFSTs whose core concrete was confined by various kind of stirrup cages, the results showed that the stirrup cages welded on the inner wall of steel tube could further improve the seismic performance of CFSTs. Zhang et al. [16] introduced the seismic performance of square SRCFSTs with internal rebars through experiment and theoretical analysis, the research results showed that higher strength of rebars will generate better seismic performance, and the cumulative damage and plastic deformation are also significantly reduced by the rebars. Zhu et al. [17] studied the hysteretic behavior of square CFSTs with internal I-shaped steel and crossed I-shaped profiled steel, it was found that the ductility coefficient of the SRCFSTs have been obviously improved by the internal profiled steel, and the axial compression ratio was the most important factor affecting the ductility and energy dissipation capacity. Liu et al. [18]-[19] investigated the seismic behavior of square CFSTs with internal I-shaped steel, and the influence of the axial compression ratio and the shear studs of I-shaped steel on the ductility coefficient and the plastic deformation capacity was studied, the results indicated that the axial compression ratio has significant influence on the seismic behavior, and the shear studs welded on the flange of I-shaped steel have negligible effect on the seismic performance. Based on the research results presented by relevant researchers, it can be found that the axial compression ratio has the greatest influence on the seismic behavior of SRCFSTs, followed by the steel ratio and diameter-to-thickness ratio, and the concrete strength has the smallest influence.

Generally, research results on the seismic behavior of SRCFSTs have revealed that the internal steel stiffeners could obviously improve the bearing capacity, stiffness and ductility, hence, it is expected that the CFSTs reinforced with internal latticed steel angles may have favorable mechanical properties, however, there are no reports on the hysteretic behavior of this composite columns. Therefore, this paper intends to study the seismic performance of the CFSTs with internal latticed steel angles via tests and finite element analysis, the parameters investigated in the test are: the diameter-thickness ratio, area of steel angles and axial compression ratio, after the test, a finite element model was established and verified by the test results, and parametric analysis was also performed using the developed finite element model.

2 Experimental programs

2.1 Material properties

2.1.1 Steel

The material properties of the steel were obtained through uniaxial tensile test according to Chinese specification of GB/T 228.1-2010 [20]. The measured material properties of steel are shown in Table 1 [21].

Table 1 Measured material properties of steel [21]

Steel	Nominal thickness (mm)	f_y/MPa	f_u/MPa	E_s/GPa
Steel tube	4	276	418	206
Steel angles	4	297	433	213
	5	283	420	208

2.1.2 Concrete

The compressive strength of the filled concrete was tested according to GB/T 50081-2019 [22], and the average compressive strength of the 150×150×150 mm concrete cubes was 32.9 MPa [21] with the young's modulus of 30750 MPa.

2.2 Specimen design

The designed diameter-to-thickness ratio (D_o/t_o) of the steel tube was between 60 and 75, which was smaller than the specified maximum value in GB 50936-2014 [23] (the specified maximum value of D_o/t_o is $135\cdot(235/f_{yo})$, which is equivalent to 115 in this paper). The height (H) of the designed specimens was 1600 mm (excluding the height of the end plate and base), the diameter (D_o) of the steel tube were 250 mm and 300 mm, and the dimensions ($b \times t_i$) of single equilateral steel angle were 40×4 mm and 50×5 mm. The size and spacing of the splicing plates, as well as the schematic diagram of the latticed steel angles were consistent with the previous study [21].

Table 2 Details of the test specimens

Specimens	D_o/mm	t_o/mm	$b \times t_i$/mm	h/mm	H/mm	n	N_o/kN
Z2504-n3	250	4	/	/	1600	0.3	794
Z2504-L4-n3	250	4	40×4	130	1600	0.3	967
Z2504-L4-n4	250	4	40×4	130	1600	0.4	1289
Z2504-L5-n3	250	4	50×5	130	1600	0.3	1082
Z3004-n3	300	4	/	/	1600	0.3	1083
Z3004-L4-n3	300	4	40×4	160	1600	0.3	1222
Z3004-L4-n4	300	4	40×4	160	1600	0.4	1630
Z3004-L5-n3	300	4	50×5	160	1600	0.3	1328

The dimensions of the designed specimens are shown in Table 2. The specimens were named according to the size and thickness of steel tube, size of steel angles, and axial compression ratio. For example, the specimen labeled "Z3004-L5-n3" represents the specimen with the exterior diameter and thickness of steel tube were 300 mm and 4 mm respectively, the size of the inner steel angles was L50×5 mm, and the axial compression ratio was 0.3 (n3 denotes 0.3). For the axial compression ratio of n, it is computed by: $n=N/N_o$, where N refers to the applied axial compressive load during test, and N_o refers to the axial compressive capacity of the equivalent short columns tested in the previous study [21].

Fig. 2 shows the schematic diagram of the test specimen. As shown in Fig.2, a steel-concrete composite box with dimension of 900×540×350 mm was designed to simulate the rigid base, the bottom of the steel tube was welded to the base to ensure the rigid connection between the steel tube and the rigid base.

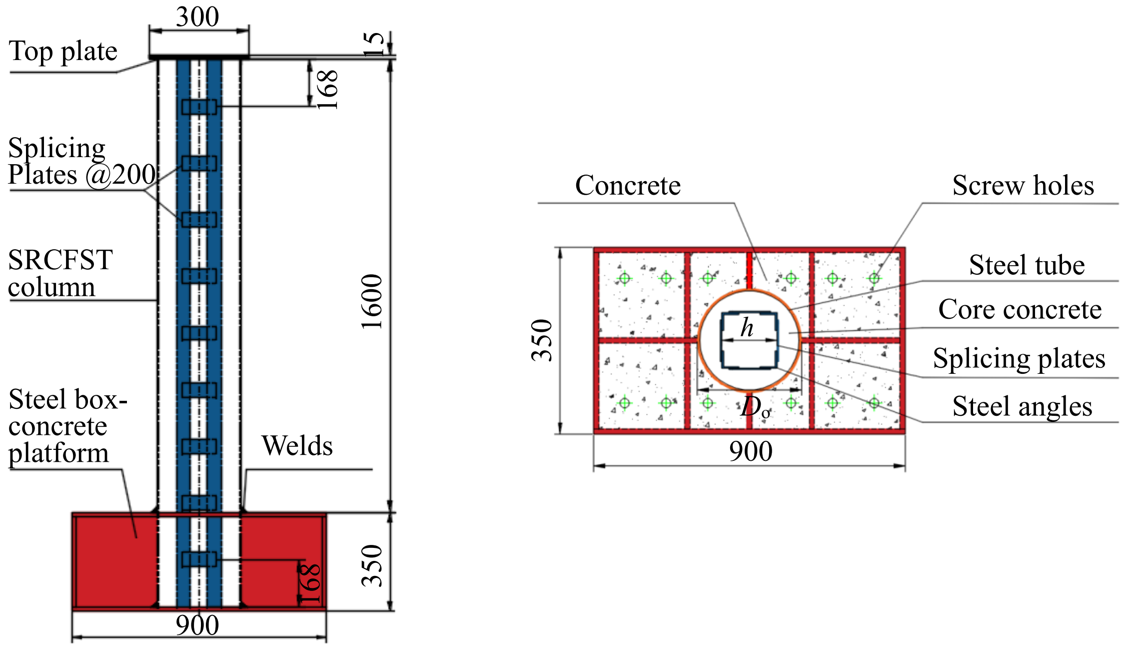

(a) Side view (b) Top view and details of the base

Fig. 2 Schematic diagrams of the test specimen (units in mm)

2.3 Test setup and loading program

All the specimens were loaded with constant axial load (vertical) and reversed cyclic load (horizontal), the vertical load was carried by the jack and the horizontal load was applied using the MTS system. The distance between the loading point and the top surface of the base is 1430 mm, which is the effective calculated height (H_o) of the tested specimens. Fig. 3 shows the diagrams of the test device. Four LVDTs were used for measuring the displacement, among which three LVDTs were arranged to measure the movement of the base, and the rest LVDT was arranged at the loading point to measure the lateral displacement. The arrangement of strain gauges is shown in Fig. 3(c), the strain gauges were arranged at 4 typical cross-sections along the height direction, which are $0.25D_o$, $0.5D_o$, $0.75D_o$ and $0.5H_o$ away from the top surface of the base, respectively. Each cross-section includes 8 measuring points, and each measuring point include one longitudinal and one hoop strain gauge.

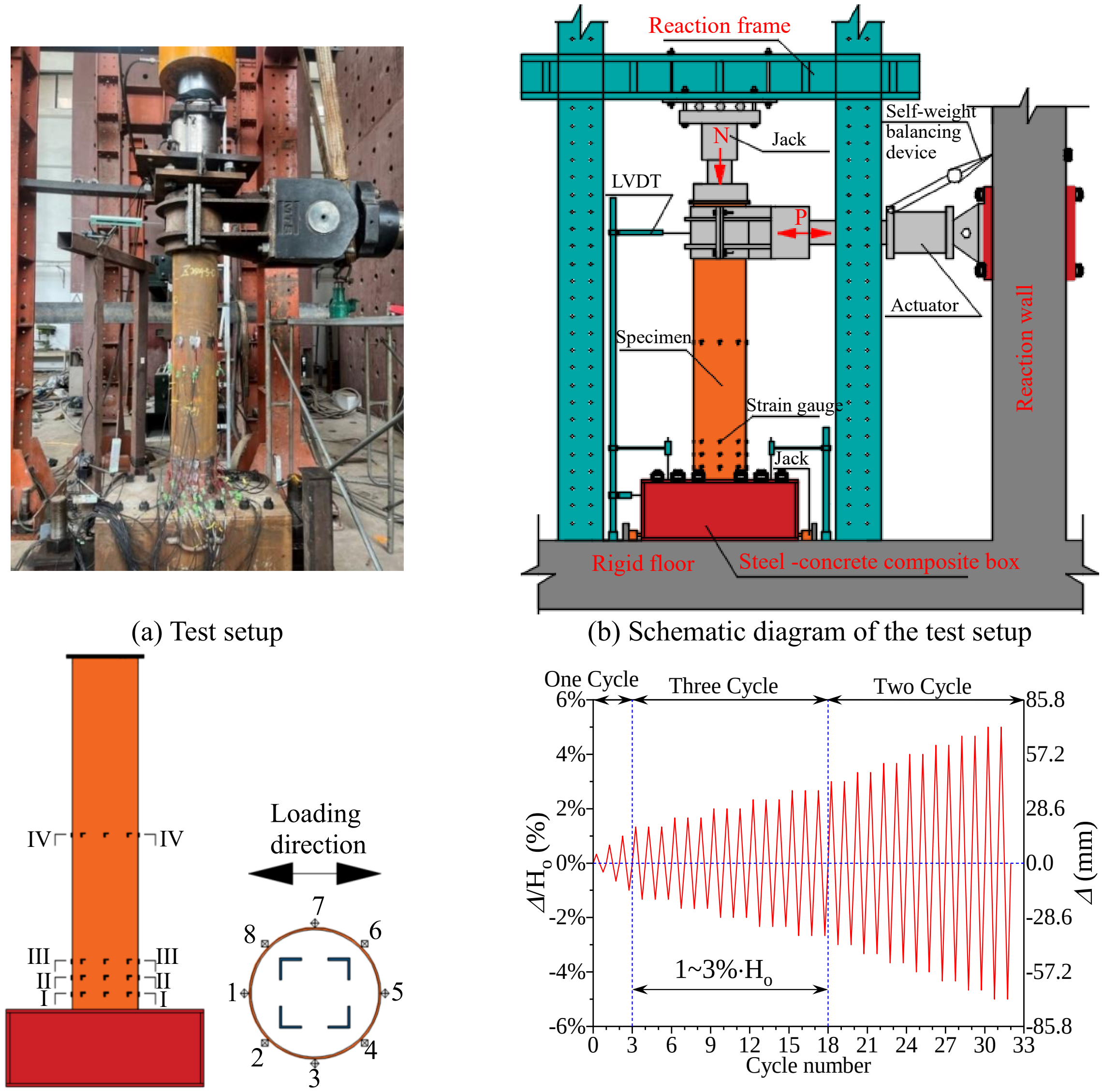

(a) Test setup

(b) Schematic diagram of the test setup

(c) Arrangement of the strain gauges

(d) Load pattern

Fig. 3 Test setup and loading pattern of the cyclic load

After the constant axial load was applied, the reversed cyclic horizontal load was applied according to the load pattern [24] shown in Fig. 3(d), where Δ is the horizontal displacement, H_o is the effective calculated height, and Δ/H_o is the drift ratio. At the beginning of the horizontal load, one cycle was applied for each drift ratio until the corresponding drift ratio reached 1%, then three cycles were applied until the drift ratio reached 3%, finally, two cycles were applied on each drift ratio until the occurrence of tube rupture or the horizontal load decreased to 85% of the ultimate load.

3 Test results and analysis

3.1 General observations

Generally, the failure modes of all test specimens were similar, as shown in Fig. 4. During the initial stage of test, there was no apparent local buckling on the steel tubes. When the drift ratio exceeds 1%, slight local buckling can be observed, which was located near the upper surface of the base, and the local buckling gradually extended to both sides with the increase of the lateral displacement, which was concentrated at $0.125D_o$ to $0.5D_o$ above the base. Finally, when the drift ratio was between 3.67% and 4.33%, the tearing of steel tube appeared due to large deformation, and the tearing failure triggered the horizontal load dropped to 85% of the ultimate load.

(a) Z2504-n3 (b) Z2504-L4-n3 (c) Z2504-L4-n4 (d) Z2504-L5-n3

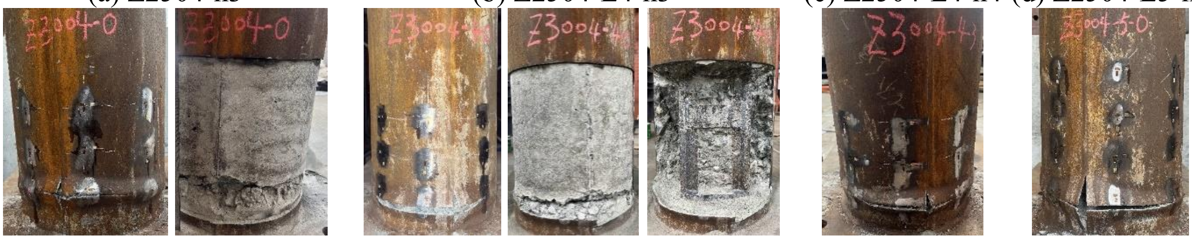

(e) Z3004-n3 (f) Z3004-L4-n3 (g) Z3004-L4-n4 (h) Z3004-L5-n3

Fig. 4 Failure modes of test specimens

For specimens Z2504-n3 (in Fig.4(a)), Z2504-L4-n3 (in Fig.4(b)), Z3004-n3 (in Fig.4(e)) and Z3004-L4-n3 (in Fig.4(f)), the failure modes of the latticed steel angles were examined. It was observed that the concrete crushed in the local buckling region, and the latticed steel angles remained intact. It is noteworthy that a slight local buckling of the latticed steel angles of specimen Z3004-L4-n3 was observed, and there has no crushing phenomenon of the concrete enclosed by the steel angles, which indicates that the latticed steel angles and the CFSTs were effectively coupled under axial load and cyclic horizontal load.

3.2 Hysteretic behaviour

Fig. 5 shows the hysteretic curves of test specimens. It was found that the hysteretic curves of the steel angles reinforced CFST specimens were full, which reveals that the specimens have excellent seismic energy dissipation capacity. However, some hysteretic curves of the columns are not symmetric, the reasons can be explained by two points: firstly, the friction force between the jack and reaction frame is uneven; secondly, the concrete damage caused by the tensile stress may affect its compression behaviour. In Fig. 5, compared with the CFST specimens, the displacement corresponding to the ultimate load of the SRCFST specimens was basically between 20 mm and 40 mm, and the ultimate capacity of the SRCFST specimens was all larger than the counterpart CFST specimens. Furthermore, by comparing the hysteretic curves of the SRCFST and CFST specimens, it was found that the latticed steel angles could provide a stronger energy dissipation capacity.

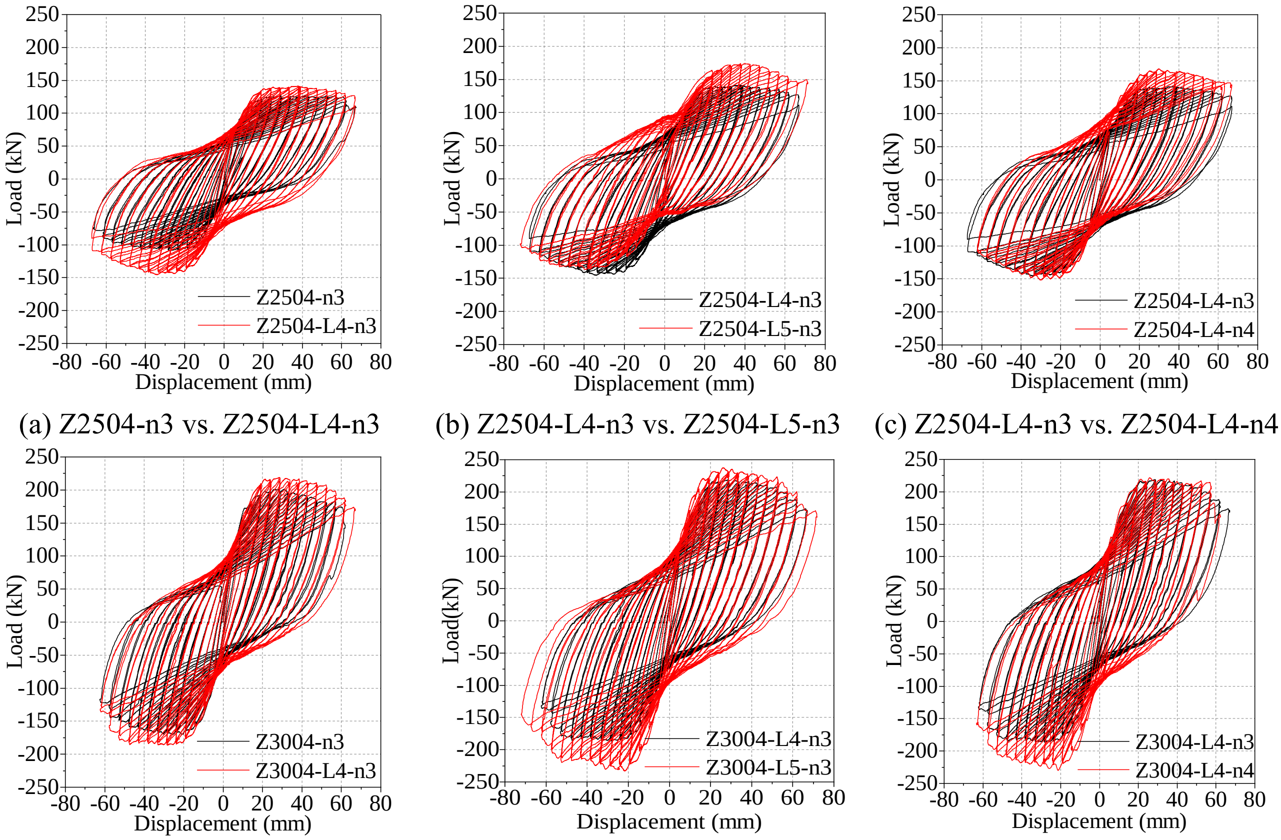

(a) Z2504-n3 vs. Z2504-L4-n3 (b) Z2504-L4-n3 vs. Z2504-L5-n3 (c) Z2504-L4-n3 vs. Z2504-L4-n4

(d) Z3004-n3 vs. Z3004-L4-n3 (e) Z3004-L4-n3 vs. Z3004-L5-n3 (f) Z3004-L4-n3 vs. Z3004-L4-n4

Fig. 5 Hysteresis curves of test specimens

As can be seen from Fig.5, it is shown that larger area of steel angles will generate higher bearing capacity and energy dissipation capacity, and the influence of the latticed steel angles is throughout the whole loading process. For the specimens under different axial compression ratios, the ultimate load increased with the increase of axial compression ratio, however, the ultimate drift ratio decreased with the increase of axial compression ratio, and the energy dissipation capacity also decreased with the increase of axial compression ratio.

3.3 Skeleton curves

The skeleton curves of the test specimens are shown in Fig. 6, the elastic stiffness and ultimate capacity obtained from the skeleton curves are shown in Fig. 7. The elastic stiffness is defined as the secant modulus between 0 and $0.4P_u$ [15], and the ultimate capacity is defined as the maximum horizontal load (P_u) during the overall loading history. The following two observations can be obtained from Fig. 7: 1) For specimens Z2504-L4-n3 and Z2504-L5-n3, compared to specimen Z2504-n3, the elastic stiffness was increased by 22.5% and 33.1%, and the ultimate capacity was increased by 14.3% and 36.5%, respectively. 2) For specimens Z3004-L4-n3 and Z3004-L5-n3, compared to specimen Z3004-n3, the elastic stiffness was increased by 9.1% and 21.6%, and the ultimate capacity was increased by 8.7% and 18.1%, respectively. The phenomenon indicates that larger area of steel angles would generate higher elastic stiffness and ultimate load, and it is more prominent for specimens with smaller diameter-to-thickness ratio.

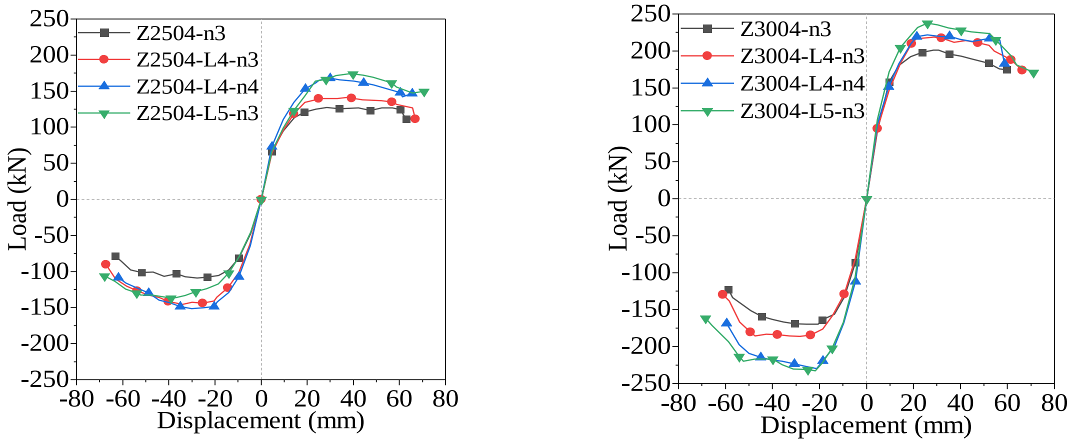

(a) D_o=250 mm, t_o=4 mm (b) D_o=300 mm, t_o=4 mm

Fig. 6 Skeleton curves of test specimens

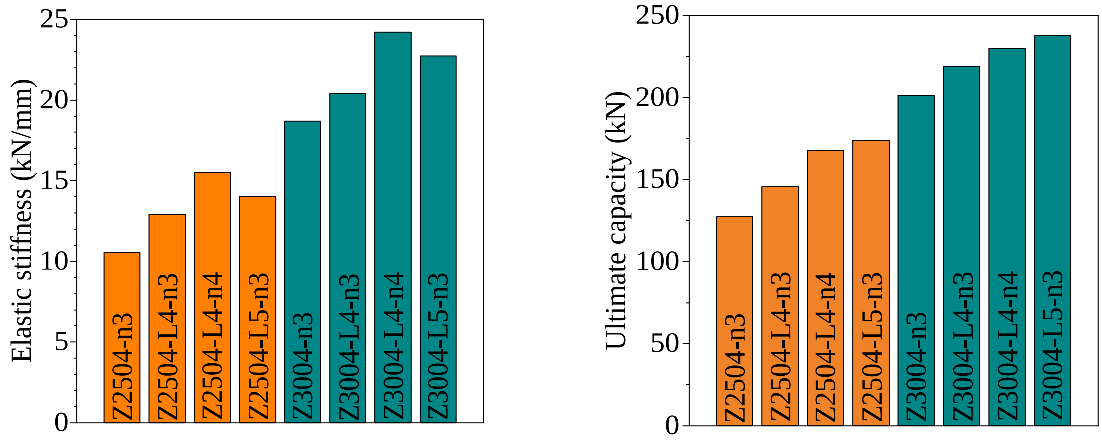

(a) The elastic stiffness (b) The ultimate capacity

Fig. 7 Comparison of the elastic stiffness and ultimate capacity

3.4 Stiffness degradation

To evaluate the stiffness degradation of the seismic behavior, the stiffness of the specimens under seismic loading is calculated by Eq. (1):

$$K_i = \frac{P_i}{\Delta_i} \tag{1}$$

Where, K_i is the stiffness of the i-th loading cycle; P_i is the ultimate load of the i-th loading cycle; Δ_i is the displacement corresponds to the ultimate load of the i-th loading cycle.

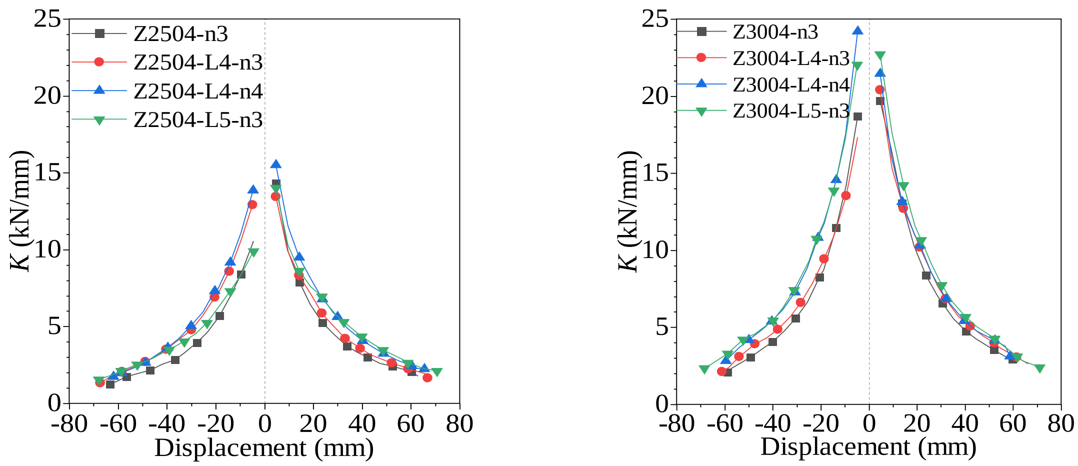

(a) D_o=250 mm, t_o=4 mm (b) D_o=300 mm, t_o=4 mm

Fig. 8 Stiffness degradation

The stiffness degradation of the tested specimens is shown in Fig. 8. The results showed that the general trend of the stiffness degradation of the test specimens is similar, and the stiffness decreased with the increase of lateral displacement, and the stiffness of the SRCFST specimens is relatively larger than the counterpart CFST specimens. The stiffness degradation can also be evaluated by the secant slope by connecting the origin points and the typical points, the calculated stiffness degradation of typical points is shown in Fig. 9. The yield point is defined by Feng's method [25], the failure point is defined as the point where the load falls to 85% of the ultimate load, and the yield stiffness, ultimate-load stiffness and failure-load stiffness are confirmed by the corresponding yield point, ultimate point and failure point, respectively.

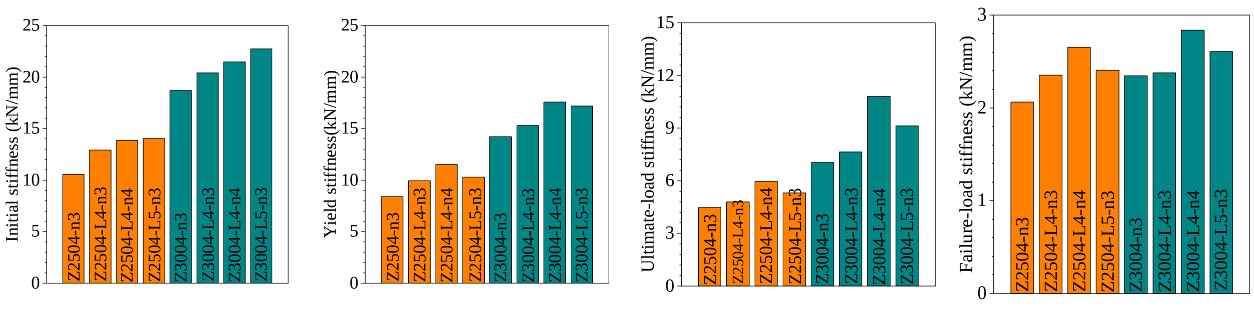

(a) Initial stiffness (b) Yield stiffness (c) Ultimate-load stiffness (d) Failure-load stiffness

Fig. 9 Comparison of the secant stiffness of typical points

Regarding the specimens with D_o of 250 mm, compared with specimen Z2504-n3, the initial stiffness, yield stiffness, ultimate-load stiffness and failure-load stiffness of specimens (Z2504-L4-n3, Z2504-L5-n3) increased by (22.5%, 33.1%), (18%, 22.2%), (7.1%, 18.5%), and (14%, 16.6%), respectively. Additionally, for the specimens with D_o of 300 mm, compared with specimen Z3004-n3, the initial stiffness, yield stiffness, ultimate-load stiffness and failure-load stiffness of specimens (Z3004-L4-n3, Z3004-L5-n3) increased by (9.1, 21.6%), (7.6%, 20.8%), (8.5%, 29.7%), and (1.2%, 11.1%), respectively. Overall, the results indicate that the latticed steel angles can improve the stiffness of specimens during the whole loading stage.

3.5 Ductility

To assess the ductility of specimens, the displacement ductility coefficient μ is calculated by Eq. (2):

$$\mu = \frac{\Delta_u}{\Delta_y} \tag{2}$$

Where, Δ_u and Δ_y are the displacement corresponding to the failure point and the yield point, respectively.

Table 3 Ductility factor of test specimens

Specimen	Load direction	Δ_y (mm)	Δ_u (mm)	μ	$\bar{\mu}$
Z2504-n3	→	9.6	63.0	6.59	6.43
	←	-9.7	-60.7	6.28	
Z2504-L4-n3	→	9.5	66.8	7.01	6.56
	←	-9.6	-58.4	6.10	
Z2504-L4-n4	→	9.6	61.4	6.39	5.96
	←	-9.7	-53.5	5.53	
Z2504-L5-n3	→	9.6	65.6	6.81	6.69
	←	-9.6	-63.2	6.57	
Z3004-n3	→	9.7	59.7	6.18	6.13
	←	-9.4	-56.9	6.08	
Z3004-L4-n3	→	9.6	62.4	6.91	6.30
	←	-9.5	-58.3	6.11	
Z3004-L4-n4	→	9.5	58.7	6.21	6.21
	←	-9.6	-59.4	6.21	
Z3004-L5-n3	→	9.5	61.7	6.49	6.34
	←	-9.5	-58.8	6.19	

The ductility coefficient of the test specimens is shown in Table 3. The average ductility coefficient $\bar{\mu}$ of the specimens is between 5.96 and 6.69, as shown in Fig. 10. In Fig. 10, it is shown that the specimens with increased area of steel angles usually have larger ductility, however, the increase of axial compression ratio will decrease the ductility. Compared with specimen Z2504-n3, the $\bar{\mu}$ of specimens Z2504-L4-n3 and Z2504-L5-n3 increased by 1.8% and 4%, respectively, compared with specimen Z3004-n3, the $\bar{\mu}$ of specimens Z3004-L4-n3 and Z3004-L5-n3 increased by 2.7% and 3.4%, respectively. It is apparent that a slight improvement in ductility was found for the SRCFST specimens.

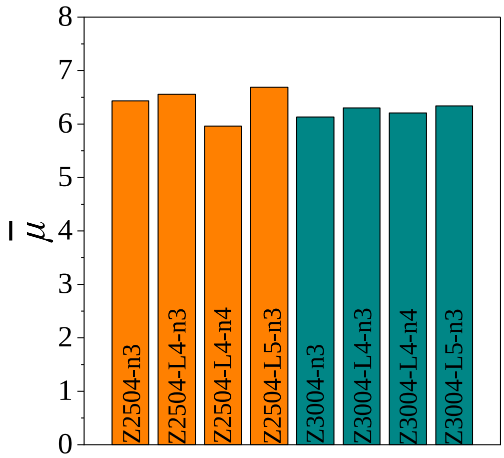

Fig. 10 Comparison of the average ductility coefficient

3.6 Energy dissipation capacity

To study the seismic performance of the specimens, some indexes, including the energy dissipation capacity ($E_{0.85}$) and equivalent viscous damping coefficient (h_e), were investigated. The energy dissipation capacity can be calculated by the area superposition of each hysteretic cycle. The energy dissipation capacity is shown in Fig. 11. When the failure occurs, the cumulative hysteretic energy dissipation values of specimens Z2504-L4-n3 and Z2504-L5-n3 were 35.4% and 56% higher than specimen Z2504-n3, and the cumulative hysteretic energy dissipation of specimens Z3004-L4-n3 and Z3004-L5-n3 were 27.4% and 50% higher than specimen Z3004-n3. In addition, the influence of the axial compression ratio on the cumulative hysteretic energy dissipation is not apparent.

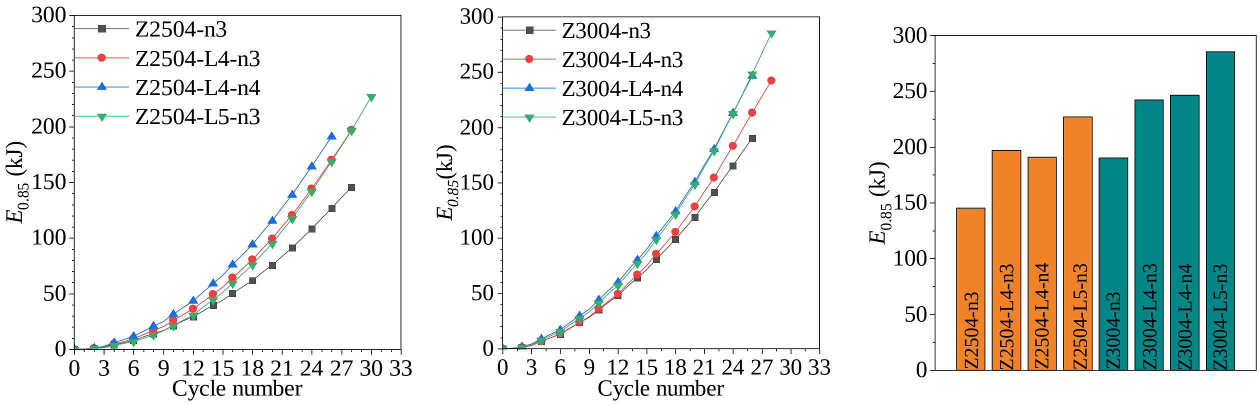

(a) D_o=250mm, t_o=4mm (b) D_o=300mm, t_o=4mm (c) At the nominal collapse of the specimens

Fig. 11 Energy dissipation capacity

The equivalent viscous damping coefficient can be calculated by Eq. (3):

$$h_e = \frac{1}{2\pi} \frac{S_{ABCDA}}{S_{(\Delta OBE+\Delta ODF)}} \tag{3}$$

Where, S_{ABCDA} is the area of the hysteretic curve of *ABCD* (the orange region), and $S_{(\Delta OBE+\Delta ODF)}$ is the total area of ΔOBE and ΔOFD (the shadow region), as indicated in Fig. 12(a).

The relationship of h_e with respect to the lateral displacement are plotted in Fig. 12(b) and (c). Obviously, for specimens with D_o of 250 mm, the maximum h_e varied from 0.25 and 0.30; for specimens with D_o of 300 mm, the maximum h_e varied from 0.22 to 0.26.

For specimens with D_o of 250 mm, compared with specimen Z2504-n3, the maximum h_e of specimens Z2504-L4-n3 and Z2504-L5-n3 increased by 15.2% and 9.0%, respectively. For specimens with D_o of 300 mm, compared with specimen Z3004-n3, the maximum h_e of specimens Z3004-L4-n3 and Z3004-L5-n3 increased by 9.8% and 16.1%, respectively. Furthermore, the improvement on the maximum h_e of the SRCFST specimens is relatively obvious than the CFST specimens at the later loading stage.

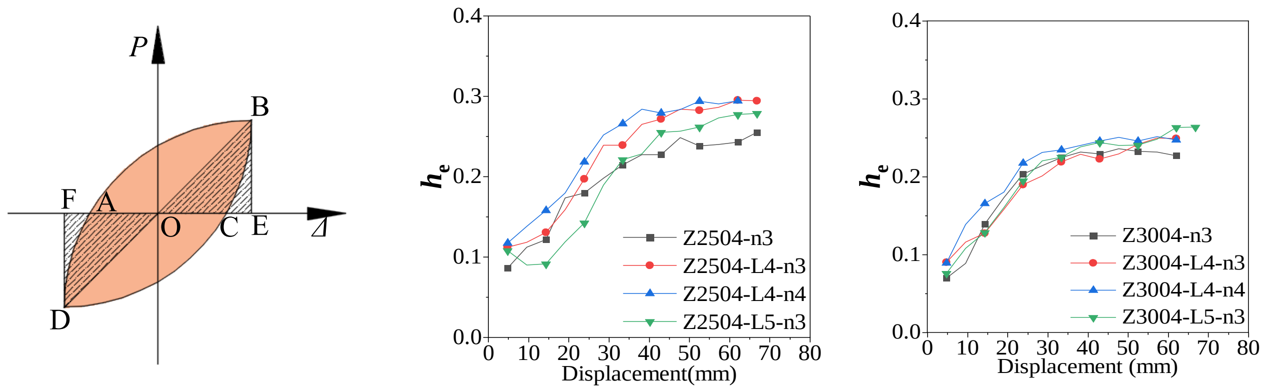

(a) Definition of h_e (b) D_o=250 mm, t_o=4 mm (c) D_o=300 mm, t_o=4 mm

Fig. 12 Equivalent viscous damping coefficient

3.7 Strain analysis

The comparison of the measured strain data is shown in Fig. 13. The longitudinal strain of the steel tube is shown in Fig. 13(a) and Fig. 13(b), it is shown that the longitudinal strain increases with the height decreases. When the drift ratio increased to 0.67%, the strain of the plastic hinge region was relatively large and exceed the yield strain (1300 με). For the hoop strain of steel tube, as indicated in Fig. 13(c) to Fig. 13(f), the hoop strain developed rapidly within the height of $0.25D_o$~$0.5D_o$, and the local deformation region observed in the experiment is also within the height of $0.25D_o$, which is consistent with the test strain. Most importantly, the development speed of the hoop strain of the SRCFST specimens has been delayed, which indicated that the existence of the steel angles reduced the deformation of steel tube. Additionally, for the hoop strain under different axial compression ratios, Fig. 13(g) and Fig .13(h) revealed that the hoop strain increased significantly at the height of $0.25D_o$~$0.5D_o$.

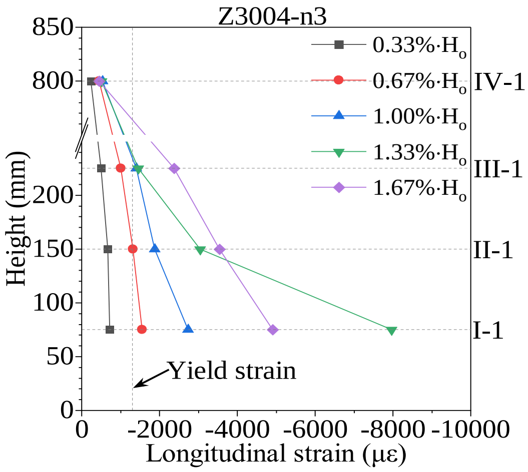

(a) Longitudinal strain of Z3004-n3 (point1)

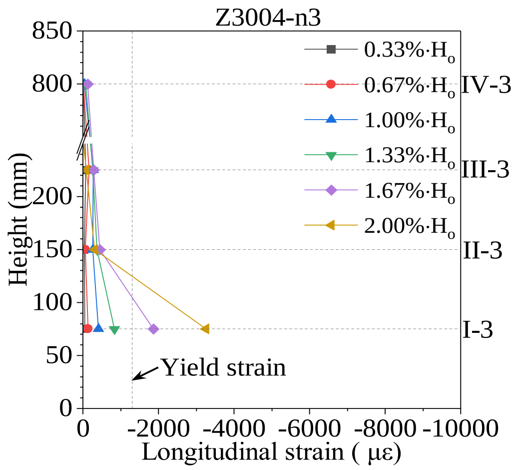

(b) Longitudinal strain of Z3004-n3 (point3)

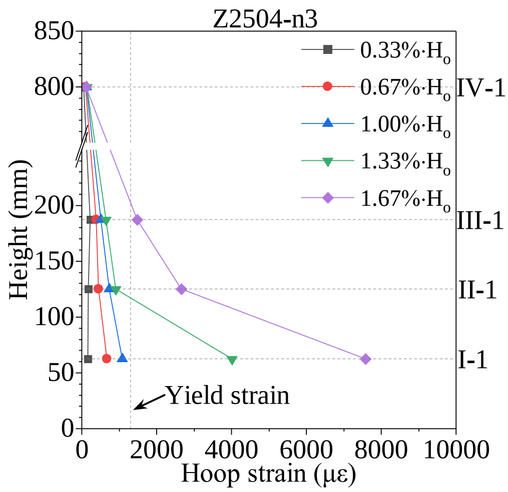

(c) Hoop strain of Z2504-n3 (point1)

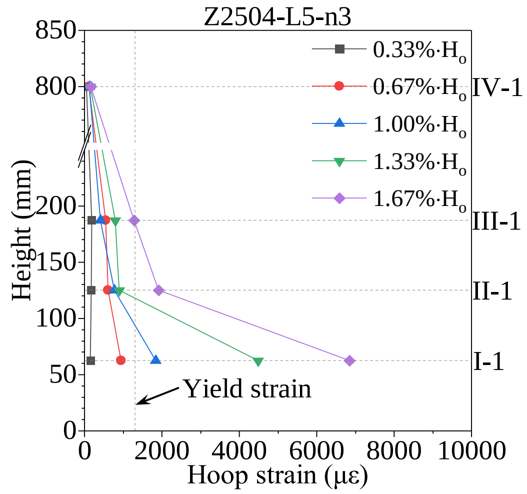

(d) Hoop strain of Z2504-L5-n3 (point1)

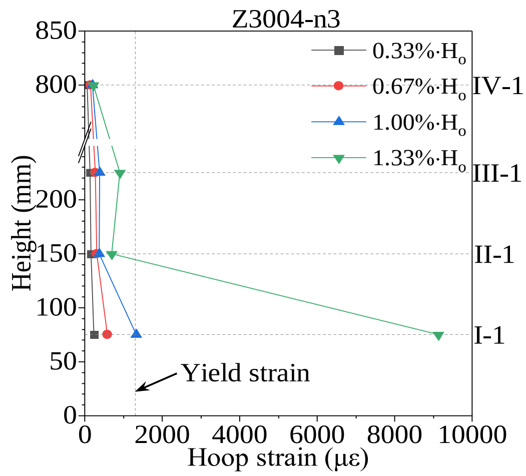

(e) Hoop strain of Z3004-n3 (point1)

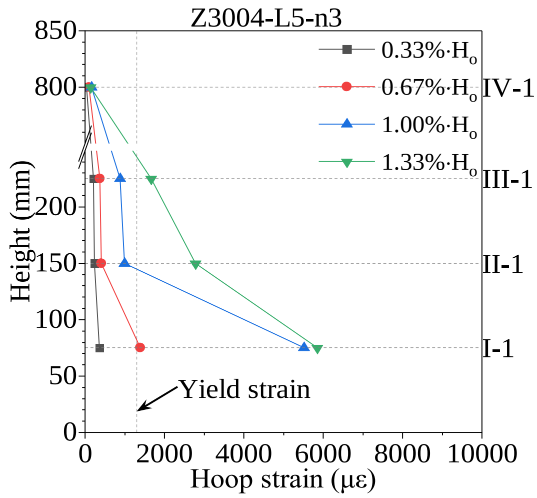

(f) Hoop strain of Z3004-L5-n3 (point1)

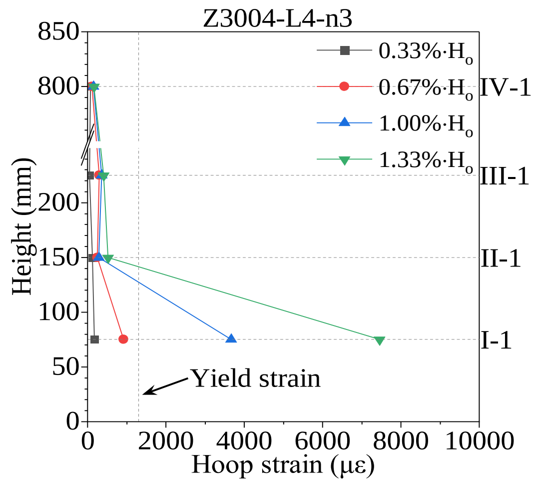

(g) Hoop strain of Z3004-L4-n3 (point1)

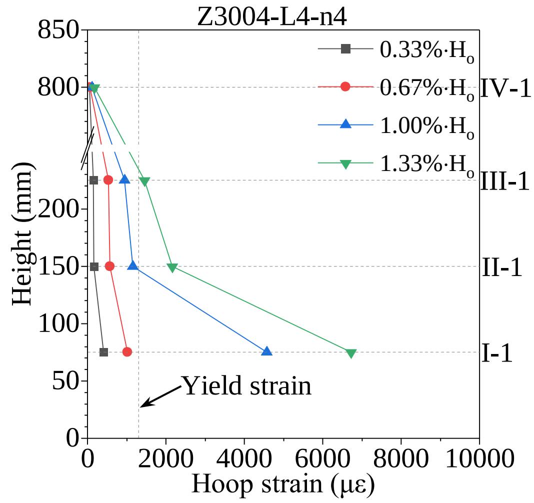

(g) Hoop strain of Z3004-L4-n4 (point1)

Fig. 13 Measured strain of steel tube

4 Finite Element Analysis

To further study the seismic behavior of the SRCFST specimens, the ABAQUS 6.14 [26] software was used to enlarge the experimental database, and the finite element (FE) models were developed considering the nonlinearity of material and geometry. The FE results were compared with the experimental results to verify the accuracy of established FE model. Finally, the FE models were further used to carry out parametric analysis.

4.1 Development of the FE modelling

4.1.1 Constitutive models of materials

The FE model consists of five parts: steel tube, concrete, steel angles, splicing plates and end plates, and the kinematic hardening model [27] was used to express the constitutive model of steel tube, steel angles. The used yield strength, ultimate strength and elastic modulus of steel are shown in Table 1. In the FE model, the concrete damage plasticity model was used to simulate the concrete, the compressive stress-strain relationship of the confined concrete proposed by Han [28] was adopted. The end plates were built by the discrete rigid shell, and the reference point (RP) was used to apply the displacement load.

4.1.2 Element types and meshes

The eight-node solid element (C3D8R) was used for the concrete, steel angles and splicing plates, while the steel tube was established by the four-node shell element (S4R) [29]-[30]. The meshing density was analysed to consider the accuracy and efficiency. The effective element size was chosen by assessing the peak load of specimen Z2504-n3, and it was found that the element size of $0.1D_o$ could provide adequate computational accuracy. To balance the calculation speed and precision, the mesh size of $0.1D_o$ was used at the bottom of the column, and 70 mm mesh size was used for the other regions. The detailed mesh of the FE model is shown in Fig. 14.

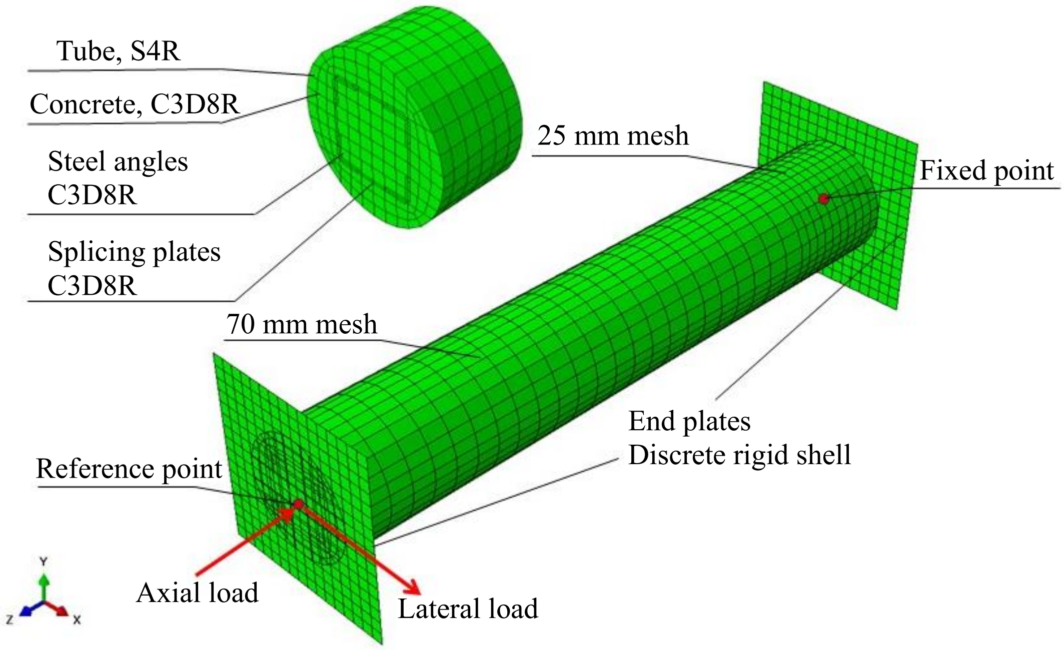

Fig. 14 Developed finite element model

4.1.3 Interactions and boundary conditions

The Coulomb friction with coefficient of 0.3 [31] and hard contact were used for the interface between the concrete and steel tube in the tangential and normal directions. The "embedded region" option was used to simulate the interactions between the concrete and latticed steel angles. The two end plates were tied with the ends of each part (including steel tube, steel angles and concrete). One of the end plates was fixed through one reference point, and the axial compression load and the lateral displacement load were applied through the other reference point.

4.2 Verification

4.2.1 Hysteretic curves

The comparison of the hysteretic curves between FE and test results is shown in Fig. 15. It can be seen from Fig. 15 that the FE results are similar to the test results, which shows that the simulation methods can accurately reproduce the hysteretic performance of the test specimens. It can be found that the FE and test results are not exactly the same, the distinction between the FE and test results are not only due to the asymmetry the tested hysteretic curves, but also the FE method can't fully reproduce the crushing of concrete as well as the boundary conditions.

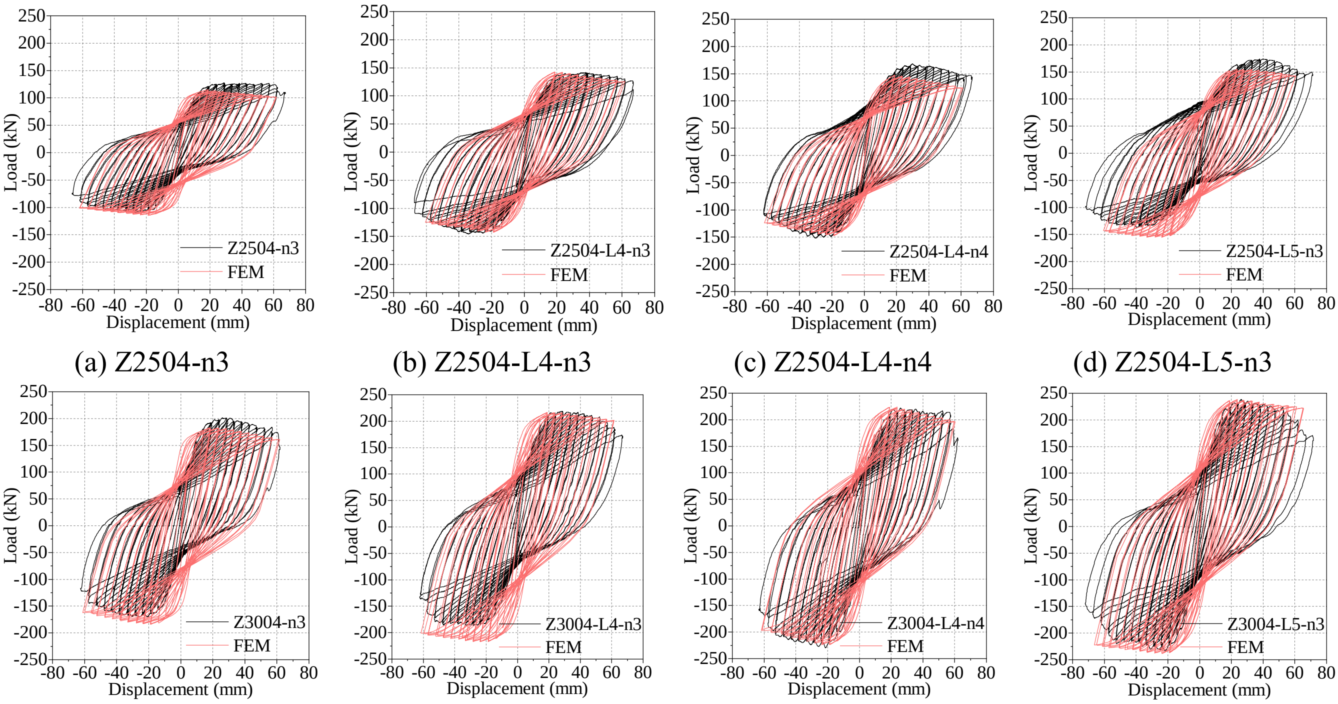

(a) Z2504-n3 (b) Z2504-L4-n3 (c) Z2504-L4-n4 (d) Z2504-L5-n3

(e) Z3004-n3 (f) Z3004-L4-n3 (g) Z3004-L4-n4 (h) Z3004-L5-n3

Fig. 15 Comparison of hysteresis curves between FE and test results

4.2.2 Skeleton curves

The comparison of the skeleton curves is shown in Fig. 16. The ultimate capacity of the FE and test results are shown in Table 4. The comparison results revealed that the deviation of the ultimate capacity varies from -12.2% to +13.3%, and the average value of $P_{\text{u-FEM}}/P_{\text{u-TEST}}$ was 0.995, with the corresponding COV was 7.6%, which indicates that the finite element model could accurately reflect the seismic performance of the tested specimens.

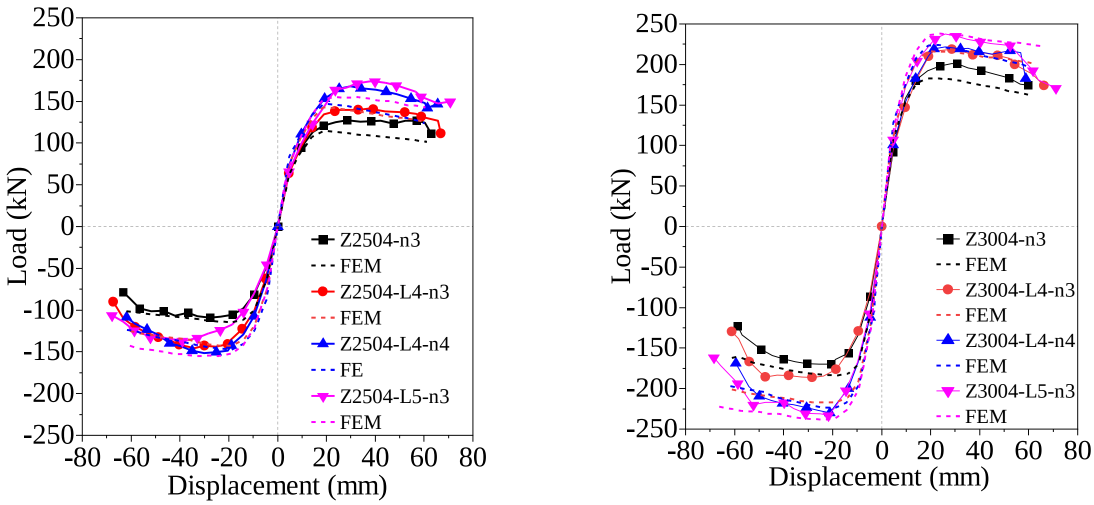

(a) D_o=250 mm, t_o=4 mm (b) D_o=300 mm, t_o=4 mm

Fig. 16 Comparison of skeleton curves between FE and test results

Table 4 Comparison of ultimate load

Specimen	Loading direction	$P_{u\text{-TSET}}$ (kN)	$P_{u\text{-FEM}}$ (kN)	$P_{u\text{-FEM}}/P_{u\text{-TSET}}$
Z2504-n3	→	127.5	114.9	0.901
	←	-109.3	-114.6	1.048
Z2504-L4-n3	→	141.6	142.4	1.006
	←	-145.7	-142.7	0.979
Z2504-L4-n4	→	167.8	147.4	0.878
	←	-151.7	-147.3	0.971
Z2504-L5-n3	→	174.0	154.9	0.890
	←	-136.8	-154.9	1.132
Z3004-n3	→	201.3	182.9	0.909
	←	-170.1	-183.7	1.080
Z3004-L4-n3	→	218.9	216.6	0.989
	←	-186.4	-211.2	1.133
Z3004-L4-n4	→	221.6	223.8	1.010
	←	-229.9	-223.8	0.973
Z3004-L5-n3	→	237.7	236.9	0.997
	←	-233.0	-238.4	1.023
			Mean	0.995
			COV	7.6%

4.2.3 Typical phenomenon

Fig. 17 shows the comparison of failure modes. Fig. 17(a) shows the comparison of steel tubes, it can be seen from Fig. 17(a) that the position of local buckling of the FE results is basically consistent with the test results. The buckling of the latticed steel angles and steel tube are shown in Fig. 17(b) and Fig. 17(c), the stress distribution can be used to evaluate the local buckling of the latticed steel angles and the fracture of the steel tube. The positions of the highest stresses occur at the center point of the local buckling region, which is consistent with the experimental failure region of the steel tube and steel angles.

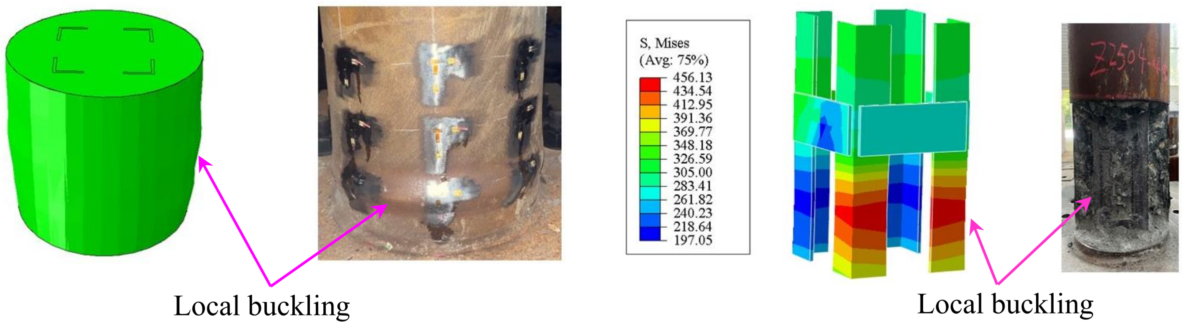

(a) Local buckling of steel tube (b) Local buckling of steel angles

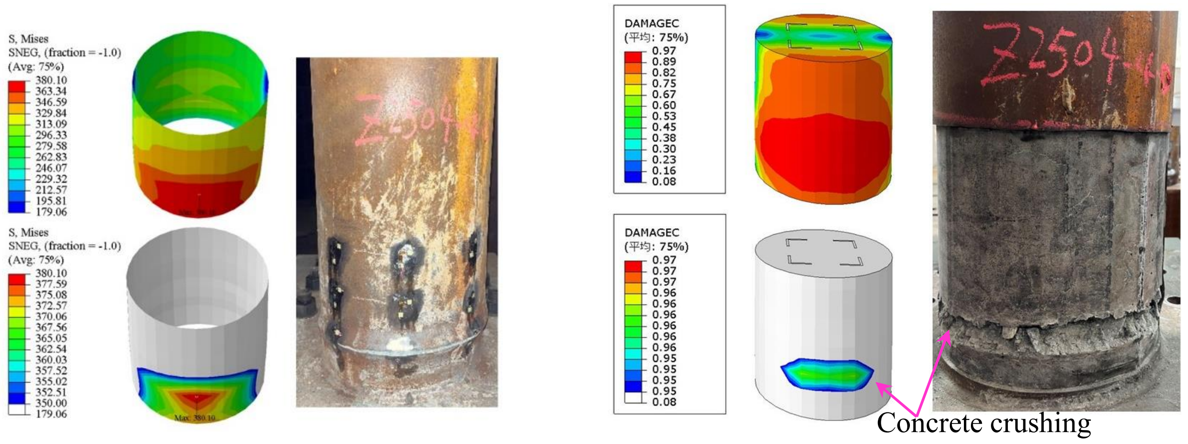

(c) Fracture of steel tube (d) Concrete crushing

Fig. 17 Comparison of failure modes

In the test results, the concrete located near the bottom was crushed, as shown in Fig. 17(d). In the FE results, the damage of concrete can be revealed by the factor of DAMAGEC, and the concrete can be considered as completely damaged when DAMAGEC>0.95[24]. In Fig. 17(d), it is shown that the damage region of concrete of the FE results is basically consistent with the experimental results.

4.2.4 Parametric analysis

In this paper, the influence of the axial compression ratio (n=0.2~0.6), the thickness of steel tube (t_o=3~6 mm) and the dimensions of steel angles (L30×3 mm~L60×6 mm) were analyzed so as to further understand the influence of main parameters on the seismic behaviour.

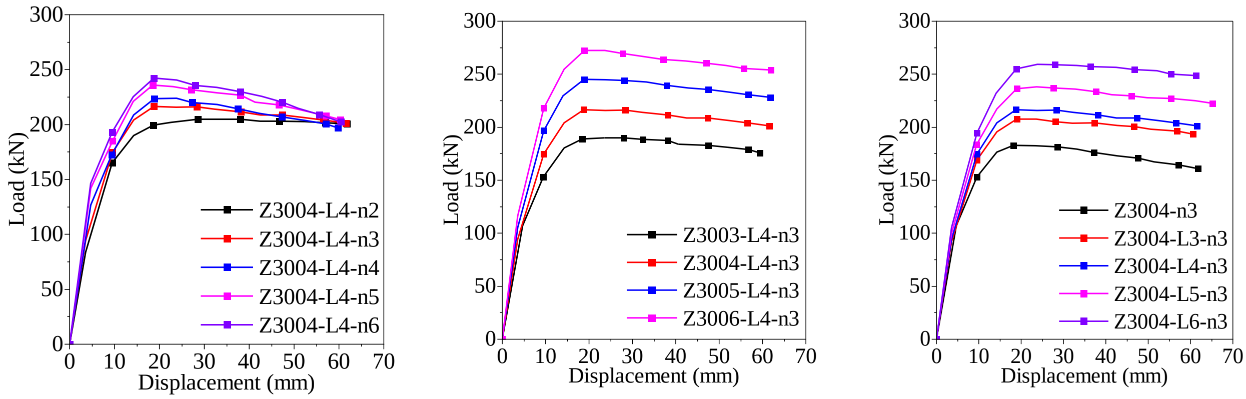

(a) Axial compression ratio (b) Thicknesses of steel tube (c) Dimensions of steel angles

Fig. 18 Influence of different parameters on the skeleton curves

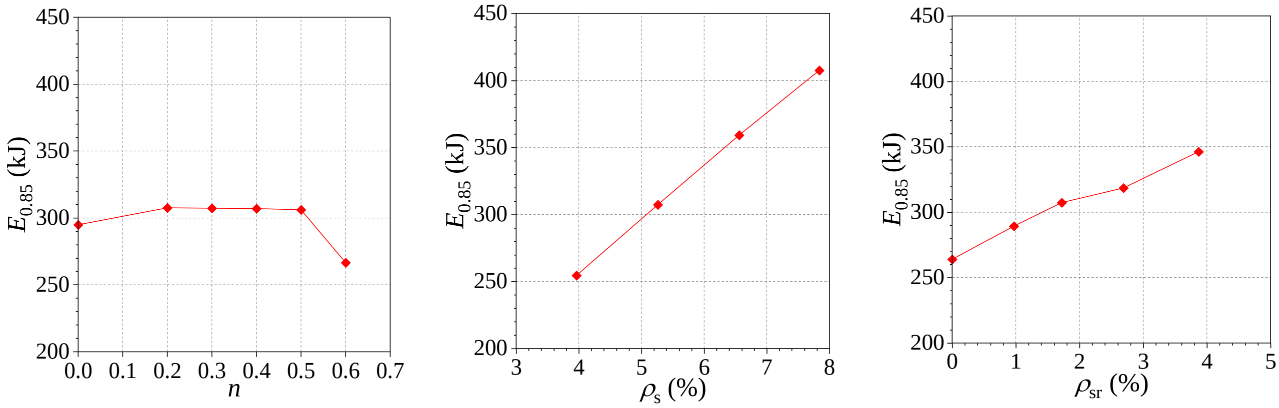

(a) Axial compression ratio (b) Thicknesses of steel tube (c) Dimensions of steel angles

Fig. 19 Influence of different parameters on the accumulated energy dissipation

Fig. 18(a) and Fig. 19(a) show the influence of the axial compression ratio. Generally, the axial compression ratio has little influence on the initial stiffness, however, the axial compression ratio has a significant influence on the ultimate load and the behaviour after the ultimate load. In Fig. 18(a), it is shown that the descending section of the skeleton curves decrease rapidly with the increase of axial compression ratio. In Fig.19(a), by comparing the cumulative energy dissipation, it can be found that the influence of axial compression ratio on the cumulative energy dissipation is not obvious in the range of 0.2 ~ 0.5, however, when the axial compression ratio is larger than 0.5, the cumulative energy dissipation decreases rapidly.

Fig. 18(b) and Fig. 19(b) shows the influence of the thickness of steel tube, where ρ_s is the ratio of steel tube's area to the total area. It is shown that the initial stiffness and ultimate capacity increase significantly with the increase of the thickness of steel tube. The cumulative energy dissipation increased almost linearly with the increase in ρ_s, as shown in Fig.19(b).

Fig. 18(c) and Fig. 19(c) shows the influence of the area of steel angles, where ρ_{sr} represents the ratio of the steel angles' area to the total area. It can be found that the initial stiffness and ultimate capacity increase with the increase of steel angels' area, and the increase of steel angels' area is helpful to ameliorate the descending section after the ultimate load. The cumulative energy dissipation increased almost linearly with the increase of ρ_{sr}, however, the influence of ρ_{sr} is less than ρ_s.

5 Horizontal bearing capacity

The horizontal bearing capacity of the composite columns have not been reported in the existing seismic design code. In this section, based on the Chinese standard (GB 50936-2014) [23] and AISC code (ANSI/AISC 360-16) [32], the design equations for the horizontal bearing capacity of the CFSTs reinforced with inner latticed steel angles were proposed based on the contribution of latticed steel angles and steel tube.

5.1 Nominal horizontal bearing capacity

Fig. 20 illustrates the working mechanism of the composite columns, the height of the plastic hinge region is within $0.25D_o$ (the height is defined as l). Considering the influence of the plastic hinge region, the bending moment can be calculated by Eq. (4), (5) and (6). Hence, the horizontal bearing capacity can be calculated in Eq. (7):

$$M = M_N + M_P \tag{4}$$

$$M_N = N \cdot \Delta \tag{5}$$

$$M_P = P \cdot (H_o - l) \tag{6}$$

$$P = \frac{M - N\Delta}{H_o - l} \tag{7}$$

Where, P is the horizontal load; M_N is the bending moment generated by the axial load N; M_P is the bending moment generated by the load P; Δ is the displacement corresponding to the load P; H_o is the effective calculated height; l is the height of the plastic hinge region.

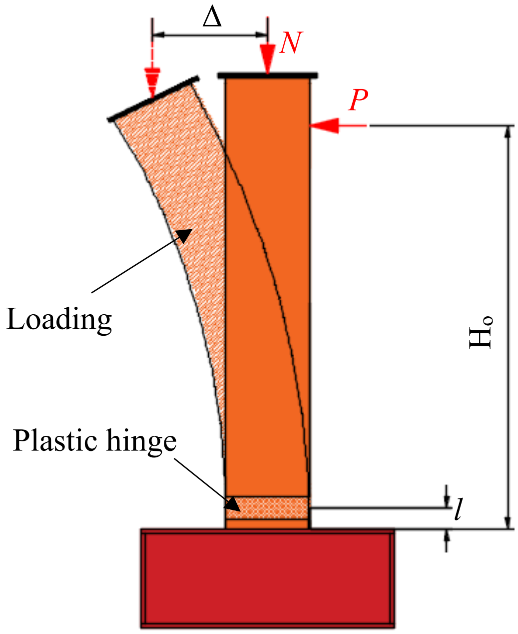

Fig. 20 Schematic diagram of the loading and plastic hinge region

5.2 Nominal bending capacity

For the CFST columns subjected to the axial compression load and bending moment, the design equations proposed by the AISC code [32] are shown in Eq. (8):

$$\begin{cases} \dfrac{N}{N_\mathrm{u}}+\dfrac{8M}{9M_\mathrm{u}}=1 & \text{for } \dfrac{N}{N_\mathrm{u}}\geq 0.2 \\ \dfrac{N}{2N_\mathrm{u}}+\dfrac{M}{M_\mathrm{u}}=1 & \text{for } \dfrac{N}{N_\mathrm{u}}<0.2 \end{cases} \tag{8}$$

Where, N is the axial load; M is the bending moment caused by the axial load N; N_u and M_u are the compressive capacity and bending capacity, respectively.

To calculate the nominal bending capacity (M) of the SRCFST columns, Eq.(8) can be converted into Eq.(9), shown as follows:

$$\begin{cases} M=\dfrac{9}{8}(1-\dfrac{N}{N_\mathrm{SR}})M_\mathrm{SR} & \text{for } \dfrac{N}{N_\mathrm{SR}}\geq 0.2 \\ M=(1-\dfrac{N}{2N_\mathrm{SR}})M_\mathrm{SR} & \text{for } \dfrac{N}{N_\mathrm{SR}}<0.2 \end{cases} \tag{9}$$

Where, N_SR and M_SR are the compressive capacity and bending capacity of the SRCFST columns, respectively; N is the axial load applied to the columns.

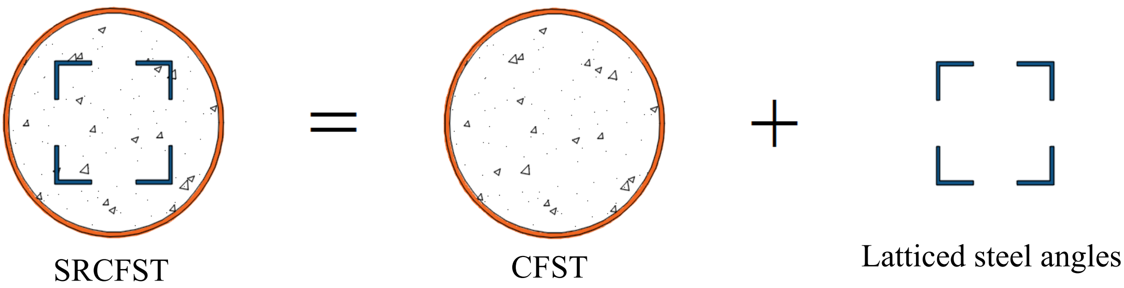

Fig. 21 Schematic diagram of the superposition method

In Fig. 21, referring to the calculation method proposed in the previous research [33]-[35], the superposition method is used to calculated the bending capacity (M_SR) of the SRCFST columns, as shown in Eq. (10):

$$M_\mathrm{SR}=M_\mathrm{o}+M_\mathrm{i} \tag{10}$$

Where, M_o and M_i are the bending capacity of the CFSTs and the latticed steel angles, respectively.

According to the design equations proposed by Han et al. [28],[36]-[37], the bending capacity of the circular CFSTs can be determined by Eqs (11)-(15), shown as follows:

$$M_\mathrm{o}=\gamma_\mathrm{m}W_\mathrm{sc}f_\mathrm{sc} \tag{11}$$

$$\gamma_\mathrm{m}=1.1+0.48\ln(\xi+0.1) \tag{12}$$

$$f_{sc} = (1.14 + 1.02\xi) \cdot f_{ck} \tag{13}$$

$$\xi = \frac{A_{so} f_{yo}}{A_c f_{ck}} \tag{14}$$

$$W_{sc} = \pi D_o^3 / 32 \tag{15}$$

Where, γ_m is the coefficient of bending capacity; W_{sc} is the overall section modulus of circular CFSTs; f_{sc} is the composite compressive strength of circular CFSTs [28]; ξ is the confinement factor; f_{ck} is the characteristic compressive strength of concrete; f_{yo} is the yield strength of steel; A_{so} and A_c are the cross-sectional area of steel tube and concrete, respectively.

Angle section members are prone to global and local buckling, and their bearing capacities would be significantly reduced [38]. However, for the bending capacity of the steel angles (M_i) which are embed into the CFSTs, the global and local buckling deformation behaviour are neglected for two main reasons: 1) Due to the connection of the splicing plates, the overall and local deformation are restrained to a certain extent; 2) The local deformation is also restrained by the surrounding concrete. Therefore, the global and local buckling deformation behaviour of the latticed steel angles are neglected when calculating M_i [39]. In this paper, the full section yielding of the maximum tensile or compressive side of the latticed steel angles are considered when calculating M_i [39], the schematic diagram of the stress distribution is shown in Fig. 22[39]. The bending capacity of the steel angles is given in Eqs. (16) and (17) [39]:

$$M_i = \frac{1}{2} A_{si} f_{yi} (h - 2h_o) \tag{16}$$

$$h_o = \frac{bt_i^2 + b^2 t_i - t_i^3}{2[b^2 - (b - t_i)^2]} \tag{17}$$

Where, A_{si} is the cross-sectional area of steel angles; h_o is the distance between the centroid and outer edge of the equilateral steel angle.

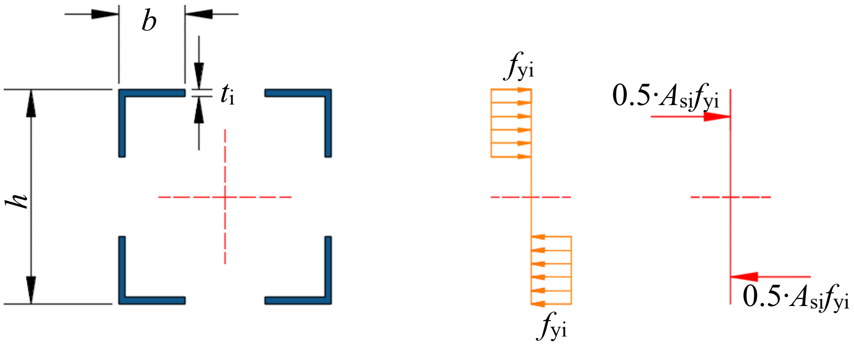

Fig. 22 Stress distributions of the latticed steel angles under full section yielding [39]

Referring the calculation method proposed in the previous research [40], the design equations for the compressive capacity of the SRCFST specimens are obtained by Eqs. (18)-(20):

$$N_{\mathrm{SR}} = (1+\rho e^{-0.745\xi_{\mathrm{s}}})\cdot(1+1.7\xi_{\mathrm{s}})\,A_{\mathrm{c}}\,f_{\mathrm{c}}' \tag{18}$$

$$\xi_{\mathrm{s}} = \frac{A_{\mathrm{so}}\,f_{\mathrm{yo}}}{A_{\mathrm{c}}\,f_{\mathrm{c}}'} \tag{19}$$

$$\rho = \frac{A_{\mathrm{si}}\,f_{\mathrm{yi}}}{A_{\mathrm{c}}\,f_{\mathrm{ck}}} \tag{20}$$

Where, ρ is the structural steel index; ξ_{s} is confinement factor; f_{c}' is the cylinder compressive strength of concrete.

5.3 Modified calculation method of the bending capacity

In AISC 360-16 [32], the compression-bending capacity is calculated by a simplified interaction curve, showing a high degree of conservation [35]. In fact, the bending capacity still increases with the increase of axial compression due to the confining effect of steel tube. In order to modify the calculation method, the correction equations for the bending capacity of the SRCFST columns were proposed from the aspects of the structural steel index (ρ), confinement factor (ξ_{s}) and axial compression ratio (n).

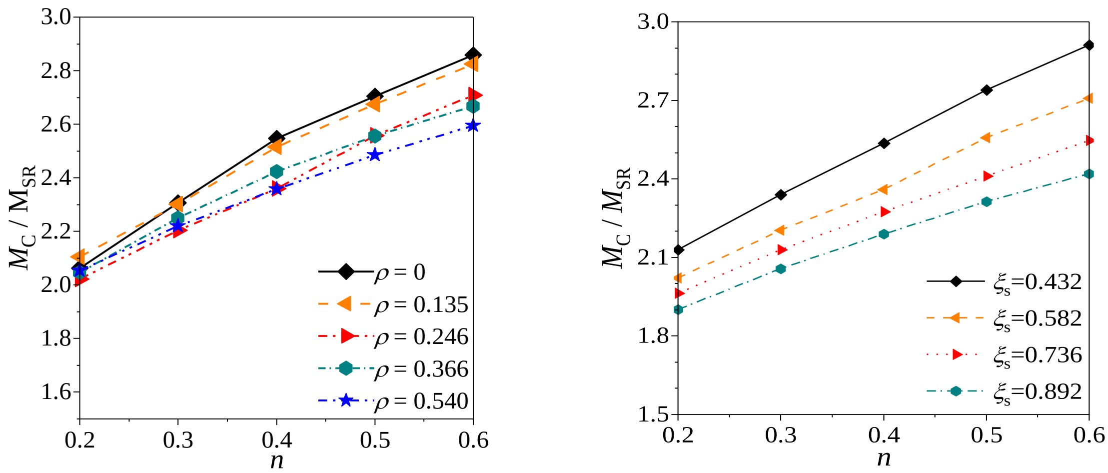

(a) Different area of steel angles (b) Different thickness of steel tube

Fig. 23 Influence of the axial compression ratio on the bending capacity

The bending capacity of the CFST specimens was first investigated. Selecting specimen Z3004-n3 as the basic parameter, the relationship between the bending capacity and the structural steel index was studied, as shown in Fig. 23(a). It can be seen that the slope (k) of the trend line decreased with the increase of structural steel index (ρ), and the linear relationship between ρ and k can be obtained as follows:

$$k = -1.181\rho + 1.988 \tag{21}$$

Base on the bending capacity of specimen Z3004-n3, the quantitative relationship between the axial compression ratio and bending capacity can be obtained:

$$M_{\mathrm{C}} = RM_{\mathrm{SR}} \tag{22}$$

$$R = R_{\xi_{\mathrm{s}}} \cdot R_{\mathrm{s}} \tag{23}$$

$$R_{\xi_{\mathrm{s}}} = k \cdot n + 1.701 \tag{24}$$

Where, M_{C} is the bending capacity of the SRCFST columns; R is the correction factor.

In Fig. 23(b), the linear relationship between the confinement factor ξ_{s} and the bending capacity is obvious, hence, in order to get the relationship between R_{s} and ξ_{s}, the bending capacity of the specimens with latticed steel angles of L40×4 mm was investigated, and Eq. (24) was used as the basic formula to study the influence of ξ_{s} on the bending capacity, and the linear relationship between R_{s} and ξ_{s} is obtained as follows:

Steel tube $$R_{\mathrm{s}} = (-0.239\xi_{\mathrm{s}} + 1.149) \tag{25}$$

Hence, the correction factor R is obtained as follows:

$$R = [(-1.181\rho + 1.988) \cdot n + 1.701] \cdot (-0.239\xi_{\mathrm{s}} + 1.149) \tag{26}$$

5.4 Verification

According to the calculated results of Eq. (22) and Eq. (7), the horizontal bearing capacity of the SRCFST columns can be calculated, and the comparison results are shown in Fig. 24. It can be seen that the calculated results are in good agreement with the simulated results, the maximum calculation error is controlled within 10%. Therefore, the proposed modified calculation method can be used to predict the horizontal bearing capacity.

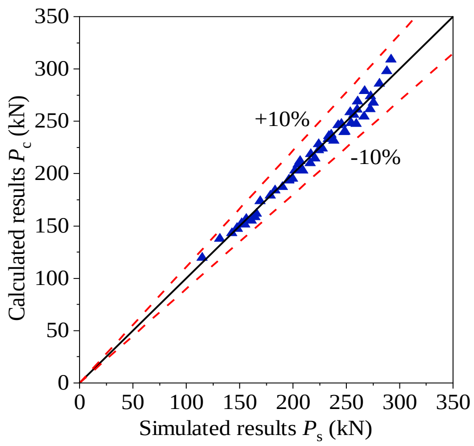

Fig. 24 Comparison of the horizontal bearing capacity

6 Conclusions

The experimental investigation and FE methods were used to study the seismic behaviour of the circular CFST columns reinforced with inner latticed steel angles. Based on the research results presented in this paper, the following conclusions can be drawn:

(1) The specimens exhibited an obvious local deformation phenomenon at the plastic-hinge region, the tearing fracture of steel tube as well as the crushing failure of concrete appeared at the plastic-hinge region;

(2) The inner latticed steel angles were able to participate in the overall loading, the increase of steel angels' area can significantly improve the elastic stiffness, ultimate load, energy dissipation capacity and ductility, however, the increase of the axial compressive ratio resulted in a reduction of the ductility.

(3) The FE results showed that the yield load and ultimate load were improved when the range of the axial compression ratio was between 0.2~0.5, however, when the axial compression ratio was larger than 0.5, the cumulative energy dissipation capacity decreased significantly.

(4) The axial compression ratio was found to have the most significant influence on the horizontal bearing capacity, and the increase of steel angels' area and steel tube's area can effectively improve the horizontal bearing capacity.

Acknowledgements

This work was supported by the Key-Area Research and Development Program of Guangdong Province (2019B111107002), the National Natural Science Foundation of China (51908016).

References

[1] Wang FC, Xie WQ, Li B, Han LH. Experimental study and design of bond behavior in concrete-filled steel tubes (CFST)[J]. Engineering Structures, 2022, 268: 114750.

[2] Wang FY, Young B, Gardner L. Compressive behaviour and design of CFDST cross-sections with stainless steel outer tubes[J]. Journal of Constructional Steel Research, 2020, 170: 105942.

[3] Han LH, Li W, Bjorhovde R. Developments and advanced applications of concrete-filled steel tubular (CFST) structures: Members[J]. Journal of constructional steel research, 2014, 100: 211-228.

[4] Wang J, Cheng XF, Yan LB, Wu C. Numerical study on I-section steel-reinforced concrete-filled steel tubes (SRCFST) under bending[J]. Engineering Structures, 2020, 225: 111276.

[5] Shi YL, Xian W, Wang WD, Li HW. Experimental performance of circular concrete-filled steel tubular members with inner profiled steel under lateral shear load [J]. Engineering Structures, 2019, 201: 109746.

[6] Wang WD, Ji SH, Xian W, Shi YL. Experimental and numerical investigations of steel-reinforced CFST members under compression-bending-shear loads[J]. Journal of Constructional Steel Research, 2021, 181: 106609.

[7] Wang WH, Li W, Song QY, Ding QR. Performance of steel-reinforced square CFST stub columns loaded in axial compression: Experiments[J]. Journal of Constructional Steel Research, 2022, 191: 107197.

[8] Xu F, Chen J, Guo Y, Ye Y. Innovative design of the world’s tallest electrical transmission towers[C]//Proceedings of the Institution of Civil Engineers-Civil Engineering, 2019, 172(5): 9-16.

[9] Xu F, Chen J, Jin WL. Experimental investigation of thin-walled CFST columns with reinforced lattice angle[J]. Thin-Walled Structures, 2014; 84: 59–67.

[10] Xu F, Chen J, Chan TM. Numerical investigation on compressive performance of CFST columns with encased built-up lattice-angles[J]. Journal of Constructional Steel Research, 2017, 137: 242–253.

[11] Gan D, Guo LH, Liu JP, Zhou XH. Seismic behavior and moment strength of tubed steel reinforced-concrete (SRC) beam-columns[J]. Journal of Constructional Steel Research, 2011, 67(10): 1516-1524.

[12] Zhou XH, Liu JP. Seismic behavior and strength of tubed steel reinforced concrete (SRC) short columns[J]. Journal of Constructional Steel Research, 2010, 66(7): 885-896.

[13] Chang X, You-Yi Wei, Yun YC. Analysis of steel-reinforced concrete-filled-steel tube (SRCFST) columns under cyclic loading[J]. Construction and Building Materials, 2012, 28(1): 88-95.

[14] Hu HS, Chen ZX, Wang HZ, Guo ZX. Seismic behavior of square spiral-confined high-strength CFST columns under high axial load ratio[J]. Engineering Structures, 2022, 252: 113600.

[15] Ding FX, Liu YC, Fei L, Lu DR, Chen J. Cyclic loading tests of stirrup cage confined concrete-filled steel tube columns under high axial pressure[J]. Engineering Structures, 2020, 221: 111048.

[16] Zhang SM, Liu JP. Seismic behavior and strength of square tube confined reinforced-concrete (STRC) columns[J]. Journal of Constructional Steel Research, 2007, 63(9): 1194-1207.

[17] Zhu MC, Liu JX, Wang QX. Experimental study of seismic behavior of square steel tubes filled with steel-reinforced high-strength concrete[J].China Civil Engineering Journal, 2011, 44(07): 55-63. (in Chinese)

[18] Liu JP, Abdullah JA, Zhang SM. Hysteretic behavior and design of square tubed reinforced and steel reinforced concrete (STRC and/or STSRC) short columns[J]. Thin-Walled Structures, 2011, 49(7): 874-888.

[19] Liu JP, Li X, Zang XZ, Chen YF, Wang XD. Hysteretic behavior and modified design of square TSRC columns with shear studs[J]. Thin-Walled Structures, 2018, 129: 265-277.

[20] GB/T 228.1-2010. Metallic materials-Tensile testing-Part 1: Method of test at room temperature. Standards Press of China, Beijing, China, 2010. (in Chinese)

[21] Wang J, Qiu WJ, Kong SC, Zhu JH. Investigation of the axial compressive behaviour of CFRP-confined circular CFST stub columns with inner latticed steel angles[J]. Composite Structures, 2022, 280: 114895.

[22] GB/T 50081-2019. Standard for test methods of concrete physical and mechanical properties. China Architecture & Building Press, Beijing, China, 2019. (in Chinese)

[23] GB 50936-2014. Technical code for concrete filled steel tubular structures. China Architecture & Building Press, Beijing, China, 2014. (in Chinese)

[24] Chen ZH, Dong SH, Du YS. Experimental study and numerical analysis on seismic performance of FRP confined high-strength rectangular concrete-filled steel tube columns[J]. Thin-Walled Structures, 2021, 162: 107560.

[25] Feng P, Qiang HL, Ye LP. Discussion and definition on yield points of materials, members and structures[J], Engineering Mechanics, 2017, 34(3): 36–46. (in Chinese)

[26] Abaqus 6.14. Abaqus Analysis User's Guide. USA: 2014.

[27] Tao Z, Wang ZB, Yu Q. Finite element modelling of concrete-filled steel stub columns under axial compression[J]. Journal of Constructional Steel Research, 2013, 89: 121–131.

[28] Han LH. Concrete Filled Steel tubular Structure-Theory and Practice, (Third Edition) [M]. Beijing: Science Press, 2016. (in Chinese).

[29] Sheehan T, Dai X H, Chan T M, Lam D. Structural response of concrete-filled elliptical steel hollow sections under eccentric compression[J]. Engineering Structures, 2012, 45: 314-323.

[30] Liu FQ, Wang YY, Chan TM. Behaviour of concrete-filled cold-formed elliptical hollow sections with varying aspect ratios[J]. Thin-walled structures, 2017, 110: 47-61.

[31] Yin F, Xue SD, Cao WL, Dong HY, Wu HP. Experimental and analytical study of seismic behavior of special-shaped multicell composite concrete-filled steel tube columns[J]. Journal of Structural Engineering, 2020, 146(1): 04019170.

[32] ANSI/AISC 360-16, Specification for Structural Steel Buildings[S], American Institute of Steel Construction, Chicago, 2016.

[33] Han LH, An YF, Roeder C, Ren QX. Performance of concrete-encased CFST box members under bending[J]. Journal of Constructional Steel Research, 2015, 106: 138-153.

[34] Wang FY, Young B, Gardner L. Testing and numerical modelling of circular CFDST cross-sections with stainless steel outer tubes in bending[J]. Engineering Structures, 2021, 247: 113170.

[35] Ma H, Qiang JQ, Xi JC, Zhao YL. Cyclic loading tests and horizontal bearing capacity of recycled concrete filled circular steel tube and profile steel composite columns[J]. Journal of Constructional Steel Research, 2022, 199: 107572.

[36] Han LH. Flexural behaviour of concrete-filled steel tubes[J]. Journal of Constructional Steel Research, 2004, 60(2): 313-337.

[37] Han LH, Lu H, Yao GH, Liao FY. Further study on the flexural behaviour of concrete-filled steel tubes[J]. Journal of Constructional Steel Research, 2006, 62(6): 554-565.

[38] Wang FY, Liang YT, Zhao O, Young B. Pin-ended press-braked S960 ultra-high strength steel angle section columns: Testing, numerical modelling and design[J]. Engineering Structures, 2021, 228: 111418.

[39] Wang J, Li JR, Li HH, Lv LY. Behaviour of square concrete-filled steel tubes reinforced with internal latticed steel angles under bending[J]. Structures, 2023, 48: 1436-1454.

[40] Wang J, Chen J, Qiu WJ, Zhu JH. Analysis of CFRP-confined CFST columns reinforced with steel angles under axial compression[J]. Journal of Constructional Steel Research, 2022, 199: 107644.

Nomenclature

The following symbols are used in this paper:

Latin upper case letters

A_{c}	Cross-sectional area of concrete;
A_{si}	Cross-sectional area of steel angles;
A_{so}	Cross-sectional area of steel tube;
D_{o}	Outer diameter of steel tube;
E_{s}	Elastic modulus of steel;
$E_{0.85}$	Cumulative hysteresis energy dissipation of nominal collapse point;
H	Height of the specimens;
$\mathrm{H_{o}}$	Calculated height of the specimens;
K	Stiffness value of the specimens;
K_{i}	Stiffness value of the *i*-th loading cycle;
M	Bending moment caused by the axial load N;
M_{C}	Bending capacity of the SRCFST columns;
M_{i}	Bending capacity of the steel angles;
M_{N}	Bending moment generated by the axial load N;
M_{o}	Bending capacity of the CFSTs;
M_{P}	Bending moment generated by the reversed cyclic load P;
M_{SR}	Pure bending capacity of the SRCFST columns;
M_{u}	Pure bending capacity;
N	Axial load;
N_{o}	Experimental axial compressive capacity in the previous study [21];
N_{SR}	Axial compressive capacity of the SRCFST columns;
N_{u}	Axial compressive capacity;
P	Horizontal load;
P_{i}	Ultimate horizontal load corresponding to the *i*-th loading cycle;
P_{u}	Maximum horizontal load;
R	Correction factor;
R_{s}	Steel tube influencing factor;
$R_{\xi s}$	Structural steel index influencing factor;
S_{ABCDA}	Area of the hysteretic curve *ABCD*;
$S_{(\Delta OBE+\Delta ODF)}$	Total area of ΔOBE and ΔOFD;
W_{sc}	Overall section modulus of the circular CFSTs;

Latin lower case letters

b	Width of single equal-leg steel angle;
f_c'	Cylinder compressive strength of concrete;
f_{ck}	Characteristic compressive strength of concrete;
f_y	Yield strength of steel;
f_u	Tensile strength of steel;
f_{sc}	Composite compressive strength of the circular CFSTs;
f_{yi}	Yield strength of steel angles;
f_{yo}	Yield strength of steel tube;
h	Distance between two adjacent steel angles;
h_e	Equivalent viscous damping coefficient;
h_o	Distance between the centroid and outer edge of the equilateral steel angle;
k	Slope of trend line;
l	Center height of the plastic hinge region;
n	Axial compression ratio;
t_o	Thickness of steel tube;
t_i	Thickness of single equal-leg steel angle;

Greek case letters

Δ	Horizontal displacement;
Δ_i	Displacement corresponding to the ultimate load of the *i*-th loading cycle;
Δ_u	Displacement corresponding to the failure point;
Δ_y	Displacement corresponding to the yield point;
γ	Residual deformation ratio;
γ_m	Coefficient of the bending capacity of circular CFSTs;
ρ	Structural steel index;
ρ_s	Ratio of steel tube's area to the total area;
ρ_{sr}	Ratio of steel angles' area to the total area;
ξ	Confinement factor of steel tube;
ξ_s	Confinement factor of steel tube;
μ	Ductility coefficient;
$\overline{\mu}$	Average ductility coefficient;